iScience

CellPress
OPEN ACCESS

Article

A high-performance Al-air fuel cell using a mesh-encapsulated anode via Al–Zn energy transfer

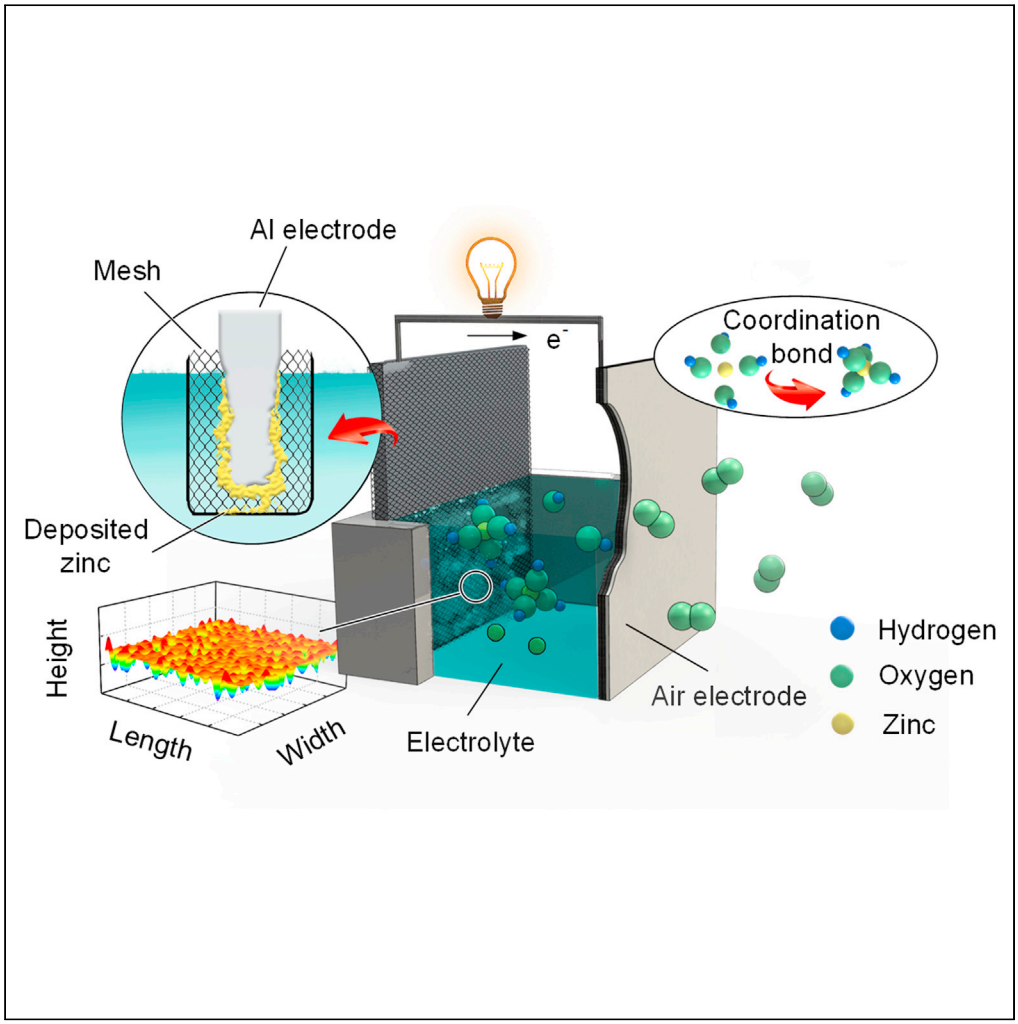

Manhui Wei, Keliang Wang, Yayu Zuo, ..., Siyuan Zhao, Yawen Li, Junfeng Chen

wangkl@bit.edu.cn

Highlights

The energy redistribution strategy is proposed to inhibit Al self-corrosion

A structure of mesh-encapsulated anode is designed to utilize the energy of dead zinc

The anode efficiency of Al-air fuel cell is up to 61.740% at 20 mA/cm^2

The capacity of Al-air fuel cell can reach 1839.842 mAh/g at 20 mA/cm^2

Wei et al., iScience *24*, 103259
November 19, 2021
https://doi.org/10.1016/j.isci.2021.103259

iScience

CellPress
OPEN ACCESS

Article

A high-performance Al-air fuel cell using a mesh-encapsulated anode via Al–Zn energy transfer

Manhui Wei,[1] Keliang Wang,[1,2,4,*] Yayu Zuo,[1] Jian Liu,[1] Pengfei Zhang,[1] Pucheng Pei,[2] Siyuan Zhao,[3] Yawen Li,[1] and Junfeng Chen[1]

SUMMARY

Aluminum-air fuel cells attract more attention because of their high specific energy, low cost, and friendly environment. However, the problems of hydrogen evolution corrosion and low anode efficiency of aluminum-air fuel cells remain unresolved. Herein, we propose an aluminum-air fuel cell using a mesh-encapsulated anode, where the energy redistribution can be achieved and the discharge performance of the fuel cell can be highly improved. The results show that the highest inhibition efficiency is 73.930% when the aluminum plate is immersed in 6 M potassium hydroxide solution containing 100% zinc oxide. The highest anode efficiency is up to 61.740% when the fuel cell using a mesh-encapsulated anode is discharged at 20 mA/cm^2, which is more than 2 times than that of no mesh, and the highest capacity can reach 1839.842 mAh/g, which is 101.623% higher than before optimization. Thus, our studies are very instructive for the large-scale application of aluminum-air fuel cells.

INTRODUCTION

As the reserves of fossil fuel are declining, new energy power generation technologies have been promoted (Chen et al., 2019; Hannula and Reiner, 2019; Jin et al., 2020; Lin et al., 2015; Wang et al., 2018a). Metal-air fuel cell (MAFC) is regarded as an excellent energy supply product because of its simple structure, low process requirements, reliable fuel sources, and stable operation without explosion hazard (Feng et al., 2020; Zhang et al., 2021; Zuo et al., 2021). Common anode metals include aluminum (Al), zinc (Zn), magnesium (Mg), lithium (Li) and calcium (Ca) (Eaves-Rathert et al., 2020; Tan et al., 2016; Wang et al., 2018b; Wu and Yu, 2018). Among them, Al has the advantages of abundant reserves, light weight, safety and reliability, and low price as an excellent energy carrier (Goel et al., 2020; Wu et al., 2020b; Zhao et al., 2020). The most important thing is that the specific mass energy of Al is 8100 mWh/g, second only to Li (Qiao et al., 2019; Tan et al., 2017); and its specific volume energy is 21,900 mWh/cm^3, which is much higher than other metals (Yu et al., 2020b). The above lays the foundation for the development of aluminum-air fuel cells (AAFC).

At present, neutral or alkaline solution is usually used as electrolyte for water-based AAFC, and stronger discharge performance is demonstrated in alkaline because the standard electrode potential of Al is lower, which is about - 2.35 V (Fan et al., 2015; Lin et al., 2015). However, once the highly reducing Al atoms meet with water molecules (H_2O) and hydroxide ions (OH^-), hydrogen (H_2) is released quickly, which reduces the utilization of Al greatly (Wu et al., 2020a, 2020b). The AAFC is limited by the Al self-corrosion, and has not been able to give full play to its advantages. In order to solve this problem, related studies have been done. Electrode alloying is an important way (Wu et al., 2020c; Yu et al., 2020a). Metal elements such as Mg or Zn with high hydrogen evolution overpotential are added to the Al surface to achieve corrosion inhibition, but the cost of it is higher and the process is more complicated. It is also a method to replace the water-based electrolyte with solid gel, but the discharge performance of fuel cells will be weakened greatly (Gao et al., 2021; Sun et al., 2021; Tian et al., 2019; Zhang et al., 2014). Another approach is to add corrosion inhibitors, and it is simple, cheap, and will not reduce fuel cell performance. Zn-containing compounds have proven to be effective corrosion inhibitors, and many studies have been carried out (Gelman et al., 2015; Mokhtar et al., 2018). For example, a fixed concentration of zinc oxide (ZnO) was added to 4 M sodium hydroxide (NaOH) solution by researchers to explore its mechanism of inhibiting hydrogen evolution from Al electrodes. Moreover, the effect of ZnO and organic acid on the corrosion resistance of the Al electrode surface was further investigated in this study (Jiang et al., 2020). On the other hand, scholars analyzed the electrochemical properties such as the equilibrium potential and corrosion current of the Al alloy (AA5052)

[1]School of Mechanical Engineering, Beijing Institute of Technology, Beijing 100081, China

[2]State Key Lab. of Automotive Safety and Energy, Tsinghua University, Beijing 100084, China

[3]Department of Building and Real Estate, The Hong Kong Polytechnic University, Hong Kong 999077, China

[4]Lead contact

*Correspondence: wangkl@bit.edu.cn

https://doi.org/10.1016/j.isci.2021.103259

electrode when putting ZnO from 1 to 8 mM into the 4 M NaOH solution.Based on this regularity, 10 mM 8-Hydroxyquinoline was added to further improve capacity and other performance parameters of the fuel cell (Zhu et al., 2019). Recently, zinc sulfate ($ZnSO_4$) has been used by researchers instead of ZnO to dissolve in alkaline solution as an inhibitor. The regularity of Al self-corrosion was studied when the concentration of $ZnSO_4$ changed from 1 to 10 mM, and sodium alginate was used in conjunction with the optimal $ZnSO_4$ concentration to further reduce the hydrogen evolution rate of Al and improve the discharge performance of the fuel cell (Yang et al., 2021).

Previous studies have promoted the development of AAFC greatly. However, the influence of the percent saturation (PS) of zinc ions (Zn^{2+}) in the electrolyte on the Al self-corrosion is still unclear. Besides, how to deal with the fallen dead zinc also needs to be further explored. In order to solve the above problems and prevent other ions from interfering with the chemical reaction, ZnO with different PS is added to potassium hydroxide (KOH) solution with different concentration. In addition, a system with two main ions of tetrahydroxyzincic acid ions [$Zn(OH)_4^{2-}$] and OH^- coexisting is obtained. Under this system, the hydrogen evolution test is performed to obtain the synergistic inhibition regularity of Zn^{2+} and OH^-. Then, electrochemical tests such as polarization behavior and impedance spectroscopy are conducted to explain the influence of Zn on the Al surface. Next, a structure of mesh-encapsulated anode that can recycle the dead zinc is designed, and the discharge experiment of fuel cells with and without a mesh is carried out to obtain performance parameters such as anode efficiency and capacity. Finally, the micro test of Al is implemented to verify the energy redistribution strategy. The purpose of this study is to explore the influence of the PS of Zn^{2+} on hydrogen inhibition and charge transfer in the fuel cell, and reuse the dead zinc with the help of a mesh to further increase the anode efficiency and capacity of the fuel cell. Therefore, it provides guidance and reference for the development of AAFC.

RESULTS AND DISCUSSION

The energy distribution law of Al electrode is shown as Equation 1. It can be seen that the utilization rate of the Al electrode can be improved only by reducing the E_H as much as possible [the hydrogen evolution reaction is shown as Equation 2] (Wang et al., 2019b, 2020b). The addition of ZnO can achieve this goal well. In this process, Zn^{2+} as the central atoms combine with OH^- in the form of coordination bonds to form $Zn(OH)_4^{2-}$ [Equation 3] (Jiang et al., 2020; Zhu et al., 2019). After that, substitution reaction will happen between Al with strong reducibility and $Zn(OH)_4^{2-}$ to obtain Zn and tetrahydroxyaluminate ions [$Al(OH)_4^-$] [Equation 4] (Jiang et al., 2020; Zhu et al., 2019). Finally, Zn adheres to the surface of the Al electrode to protect it from self-corrosion.

$$E_{Al} = E_c + E_i + E_H \quad \text{(Equation 1)}$$

Where E_{Al} is the total energy of Al; E_c is the energy consumed by Al discharge; E_i is the energy consumed by Al react with $Zn(OH)_4^{2-}$; and E_H is the energy consumed by Al self-corrosion (including hydrogen evolution and heat dissipation).

$$2Al + 6H_2O + 2OH^- \Rightarrow 2Al(OH)_4^- + 3H_2\uparrow \quad \text{(Equation 2)}$$

$$Zn^{2+} + 4OH^- \Rightarrow Zn(OH)_4^{2-} \quad \text{(Equation 3)}$$

$$2Al + 3Zn(OH)_4^{2-} \Rightarrow 2Al(OH)_4^- + 4OH^- + 3Zn \quad \text{(Equation 4)}$$

However, the Zn film is relatively loose, unstable and gravitational (Gelman et al., 2015). Furthermore, the Al is consumed gradually as the reaction progresses, whereas the Zn is accumulated gradually until falling off because of its excessive gravity. Besides, the external uncertain factors such as vibration, turbulence, and so on are also easy to make it fall off. Therefore, E_i has not been effectively used. Based on that, a structure of mesh-encapsulated anode is designed on the basis of the traditional AAFC. The mesh with a size of 1.5 × 1.5 mm is installed on the outer surface of Al electrode and has a gap on it. Considering that the mesh cannot participate in the electrochemical reaction, and must have the characteristics of good conductivity, low cost and easy maintenance, thus the high-strength and corrosion-resistant stainless steel material 06Cr19Ni10 is selected. The mesh can not only be used as a fuel tank for Al electrode, but also can better accept the fallen dead zinc and use the energy of Zn to discharge, as shown in Figure 1A. E_i can convert to E_c in this process, thereby the share of all Al electrons involved in discharge is increased indirectly, and the anode efficiency and capacity are also improved further. During the discharge process of the fuel cell, the leading role of the anode changes from Al to Zn as shown in Figure 1B.

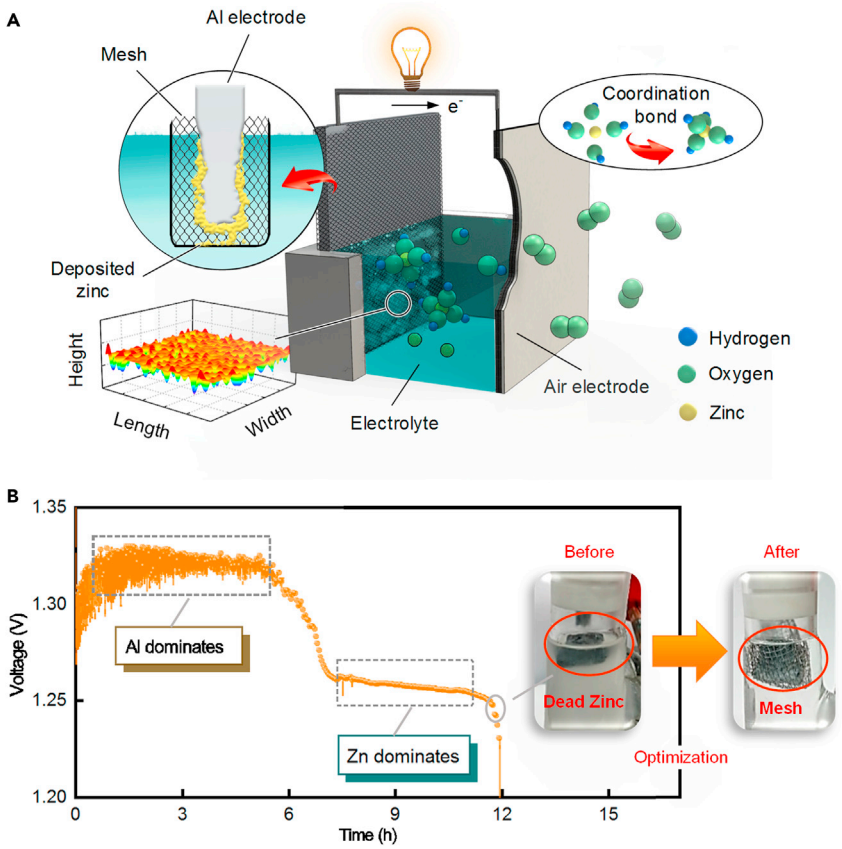

Figure 1. Proposed system

(A) AAFC using a mesh-encapsulated anode.

(B) The leading role of the anode changes from Al to Zn.

See also Figure S1.

Inhibition of Al self-corrosion

Figures 2A–2C show the systems' states and the total mass of H_2 when the Al alloy sheets are immersed in the 12 groups of electrolytes. It can be seen that the higher PS of ZnO is, the less hydrogen evolution happens on the surface of the Al alloy sheet if the concentration of OH^- is constant. This is because the higher PS of ZnO, the more stable and denser Zn film deposited on the surface of the Al electrode when the concentration of OH^- is constant, thereby the generation of H_2 is suppressed. Besides, the hydrogen evolution rate v and inhibition efficiency η_H are shown in Figures 2D and 2E. They further demonstrate the common effect of OH^- and Zn^{2+} on the inhibition of Al self-corrosion. Moreover, the lowest hydrogen evolution rate is about 1.767×10^{-3} mg/cm^{2}s and the highest inhibition efficiency is about 73.930% when the Al alloy sheet is immersed in 6 M KOH electrolyte containing 100% ZnO.

Electrochemical analysis of anode

According to the hydrogen evolution test, it can be known that the 6 M KOH electrolyte containing ZnO has a better hydrogen inhibition effect. Therefore, 6 M KOH is cited as an example, and the influence of the PS of ZnO on the hydrogen inhibition and charge transfer characteristic of the Al electrode surface is analyzed from the perspectives of open circuit potential (OCP), Tafel polarization curve (TPC) and electrochemical impedance spectroscopy (EIS).

Figure 3A shows the OCP of Al electrode immersed in 6 M KOH electrolyte containing ZnO with different PS for 500 s. A similar changing law can be seen from it: because the aluminum oxide (Al_2O_3) and other substances on the Al electrode surface block the contact between Al and solution at the beginning of immersion, the potential is negative but cannot reach the theoretical value (Wu et al., 2020b). Within 100–150 s

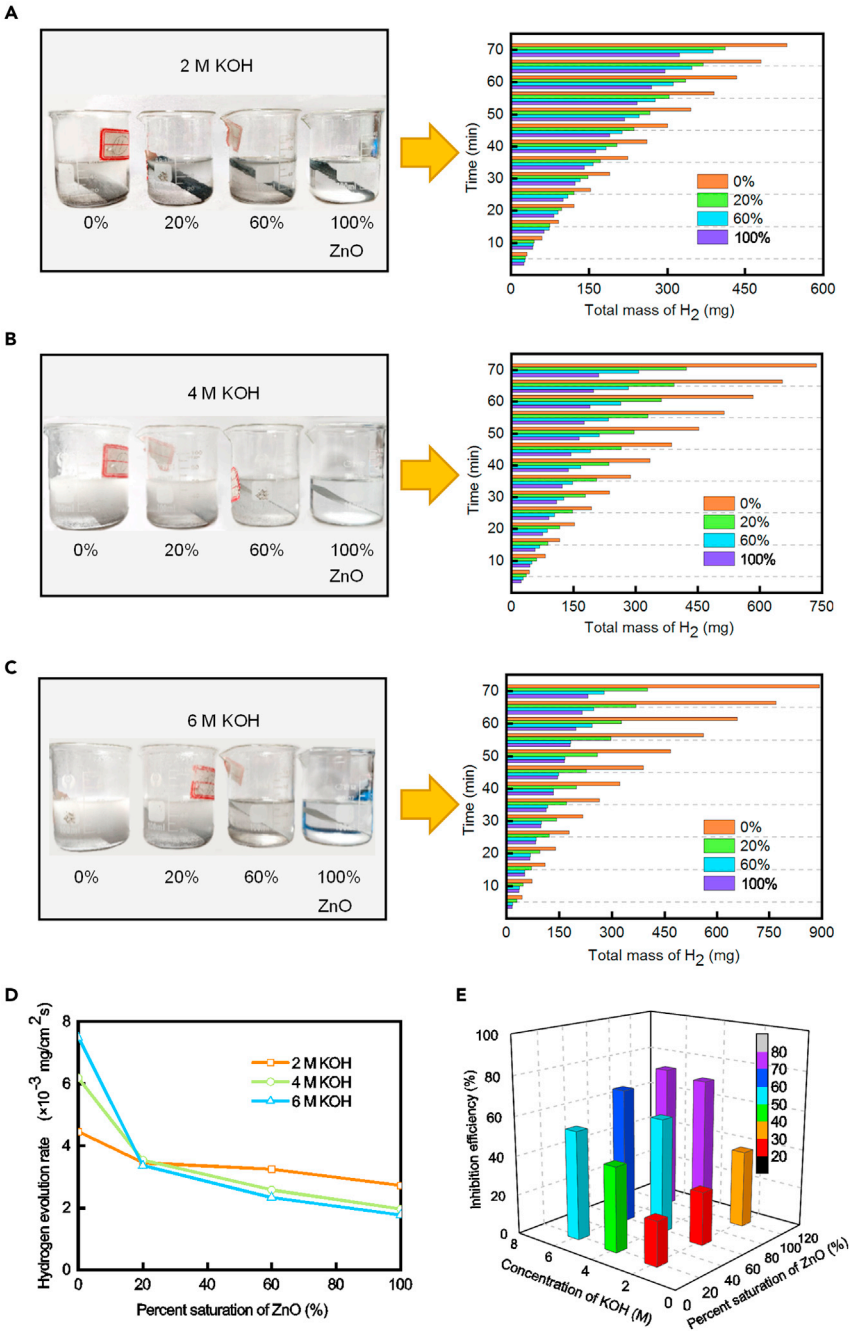

Figure 2. Hydrogen evolution test when Al immersed in KOH electrolyte with different concentration containing ZnO with different PS

(A) Hydrogen evolution when Al is immersed in the 2 M KOH electrolyte containing 0%, 20%, 60% and 100% ZnO.

(B) Hydrogen evolution when Al is immersed in the 4 M KOH electrolyte containing 0%, 20%, 60% and 100% ZnO.

(C) Hydrogen evolution when Al is immersed in the 6 M KOH electrolyte containing 0%, 20%, 60% and 100% ZnO.

(D) Hydrogen evolution rate when Al is immersed in the KOH electrolyte with different concentration containing ZnO with different PS.

(E) Inhibition efficiency when Al immersed is in the KOH electrolyte with different concentration containing ZnO with different PS.

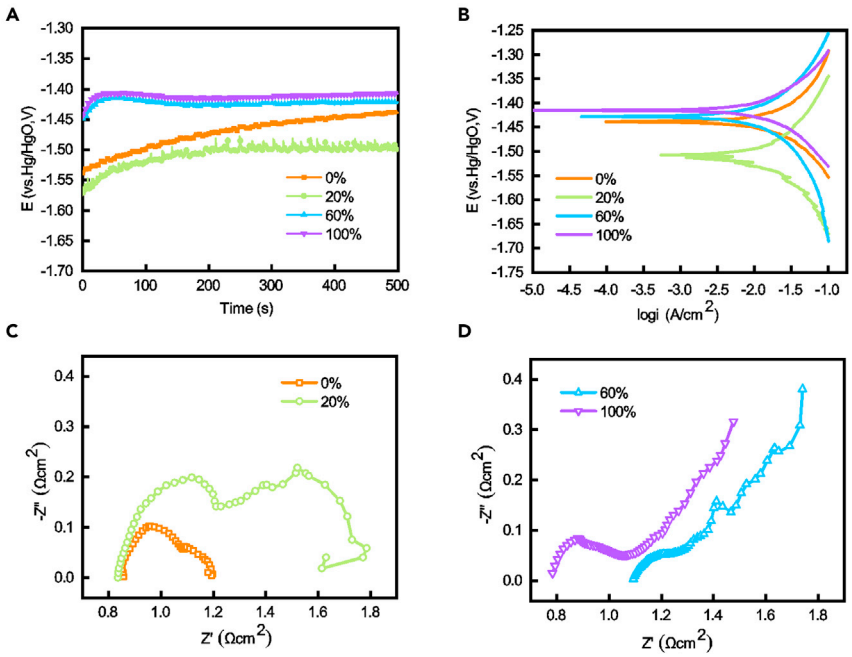

Figure 3. Electrochemical analysis of Al electrode immersed in 6 M KOH electrolyte containing ZnO with different PS

(A) The OCP of Al electrode immersed in 6 M KOH electrolyte containing 0, 20, 60, and 100% ZnO for 500 s.

(B) The TPC of Al electrode after reaching a steady state in 6 M KOH electrolyte containing 0, 20, 60, and 100% ZnO.

(C) The EIS of Al electrode after reaching a steady state in 6 M KOH electrolyte containing 0, and 20% ZnO.

(D) The EIS of Al electrode after reaching a steady state in 6 M KOH electrolyte containing 60, and 100% ZnO.

after immersion, the potential changes greatly. It is attributed to the rapid dissolution of Al_2O_3 and formation of Zn during this stage. Besides, the rapid generation and skipping of H_2 on the surface of Al electrode also has an impact on it (Yang et al., 2021). After that, the potential tends to stabilize, but the equilibrium potential of the Al electrode is different for different PS of ZnO. When ZnO is added from 0 to 20%, the potential shifts to a negative direction because of the improvement of the Al electrode surface by a small amount of generated Zn and the reduction of corrosion products (Nie et al., 2017). When the PS of ZnO is 60%, the Zn generated on the Al electrode surface becomes denser and thicker, and covers most of the area of Al. At this time, the surface of the Al electrode contains a larger proportion of Zn, which makes the potential bias toward the lower Zn of standard electrode potential instead of the higher Al, so the potential has a more obvious positive shift. When the ZnO is added to saturation, the Zn deposited on the surface of the Al electrode becomes more and the area of exposed Al becomes smaller, so the potential continues to move positively.

Figure 3B shows the TPC of Al electrode after reaching a steady state in the 6 M KOH electrolyte containing ZnO with different PS, and the corresponding polarization behavior parameters are listed in Table 1. From the view of the equilibrium potential, it shifts negatively when the PS of ZnO changes from 0 to 20%. Thereafter, it moves positively as the PS of ZnO gradually increases. This regularity is consistent with the results of the OCP test, and its reason can also be explained from them. Besides, from the perspective of the corrosion current, it gradually decreases from 38.58 to 21.08 mA/cm^2 with the increase of PS of ZnO. The reason for this regularity is that the higher PS of ZnO can make Zn deposited more uniformly and densely on the surface of the Al electrode, and a large area of exposed Al is covered. In this case, the Al self-corrosion is suppressed and the hydrogen evolution rate is reduced. This regularity is consistent with the results of the hydrogen evolution test (Wang et al., 2020a).

Figures 3C and 3D show the EIS of the Al electrode after reaching a steady state in 6 M KOH electrolyte containing ZnO with different PS. Among them, Figure 3C shows that the Nyquist diagram of the Al electrode immersed in 6 M KOH electrolyte containing 0 and 20% ZnO have similar shapes. They are composed

Table 1. Polarization behavior parameters of Al electrodes immersed in 6 M KOH electrolyte containing ZnO with different PS

PS of ZnO (%)	$-E_{corr}$ (V vs. Hg/HgO)	i_{corr} (mA/cm^2)	k_c	k_a
0	1.439	38.58	4.994	4.394
20	1.490	25.14	5.179	5.004
60	1.428	24.08	4.476	4.902
100	1.415	21.08	7.511	7.172

of a semi-circular high-frequency region and a semi-circular low-frequency region. The first semi-circle represents the process that Al atoms lose electrons and become aluminum ions (Al^{3+}) (Jiang et al., 2020). The second semi-circle represents the process of continuous production, dissolution and escape of corrosion products such as $Al(OH)_4^-$ and H_2. Because one or more unstable and weak Zn films cover the surface of the Al electrode when the PS of ZnO is 20%, the Al^{3+} is blocked one or more times during the transfer process. It causes the transfer resistance of the charge to increase, so the radius of the first semi-circle is larger under this condition. Figure 3D shows that the Nyquist diagram of Al electrode immersed in 6 M KOH electrolyte containing 60 and 100% ZnO have similar shapes. They are composed of a semi-circular high-frequency region and a linear low-frequency region. The first difference from Figure 3C is that the radius of the first semi-circle is smaller when the PS of ZnO is 60% or 100%. The reason is that the generated Zn layer is more compact and stable at this time, and will not interfere with the charge transfer at exposed Al points. The second difference is that it has an obvious diffusion area when the PS of ZnO is 60 or 100%. The reason is that the continuous deposition of Zn causes the Zn film to press tightly on the surface of Al and cover most of the area. At this time, corrosion products such as $Al(OH)_4^-$ and H_2 are drastically reduced, so the diffusion area appears.

Performance promotion of AAFC

Figures 4A–4F show the discharge performance of the AAFC. Among them, Figures 4A, 4C, and 4E show the U-I curves of the fuel cell at a current density of 0–60 mA/cm^2 in 2, 4, and 6 M KOH electrolytes containing 0, 20, 60, and 100% ZnO. They have similar characteristics, that is, when the PS of ZnO is 20%, the voltage of the fuel cell is slightly higher than 0%. But when it is increased to 60%, the voltage will become smaller, and it will be the smallest when at 100%. The reason for it is that a small amount of Zn obtained by the substitution reaction between Al and $Zn(OH)_4^{2-}$ can be attached to the surface of the Al electrode to improve its surface characteristics when the PS of ZnO is 20%, so the voltage rises slightly. However, when the PS of ZnO continues to increase to 60% or even 100%, a stable and thick Zn layer is formed, and the voltage is more biased toward the Zn element with a lower standard electrode potential, resulting in a slight drop in the fuel cell voltage.

Figures 4B, 4D, and 4F show the discharge curves of fuel cells with and without a mesh at 20 mA/cm^2 in 2, 4, and 6 M KOH electrolytes containing 0 and 100% ZnO. It can be seen from them that the addition of ZnO can improve the discharge performance, and the capacity of the fuel cell is further improved with the help of the mesh. It can also be seen from Table 2 that a mesh-encapsulated anode has the best effect on improving the discharge performance for the fuel cell in 6 M KOH electrolyte containing 100% ZnO. Among them, the anode efficiency of the fuel cell using a mesh-encapsulated anode is about 61.740%, and the fuel efficiency is about 25.915%, which are 2.016 and 2.022 times that before optimization. The capacity is about 1839.842 mAh/g, and the specific energy is about 2099.150 mWh/g, which are 101.623% and 102.258% higher than before optimization. The reason for improvement is that the Zn layer on the surface of the Al electrode is thicker and heavier, and it is easy to fall off to form dead zinc in 6 M KOH electrolyte containing 100% ZnO. With the help of mesh, more energy of dead zinc can be used. Similarly, the performance parameters of fuel cells using a mesh-encapsulated anode under the 2 and 4 M KOH electrolyte containing 100% ZnO have also been greatly improved. The only difference is that the degree of improvement is slightly different due to the different energy of dead zinc. Finally, it should be noted that when the PS of ZnO is 100%, the highest inhibition efficiency, the lowest hydrogen evolution rate, and the largest gravity of the Zn layer can be obtained. Therefore, the energy dissipated by hydrogen is the smallest, and the energy transferred from Al to Zn is the largest at this time. It means that all the fuel energy used for discharge is the most, so 100% is regarded as the best PS of ZnO.

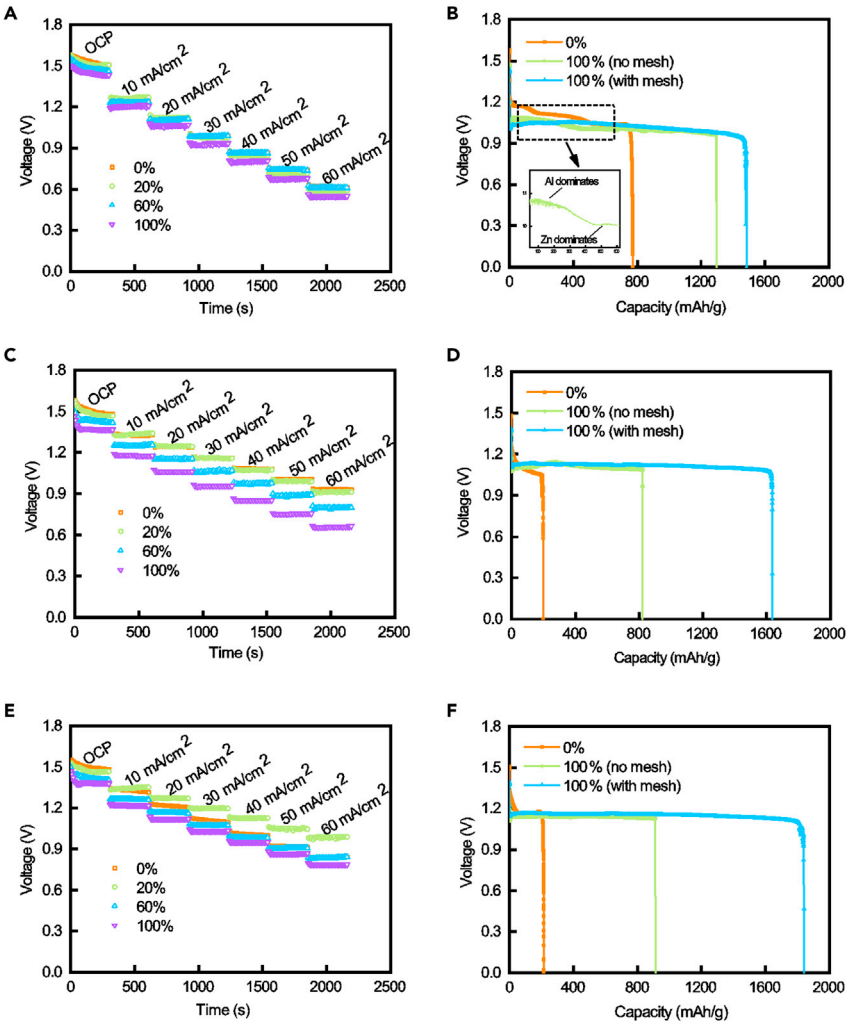

Figure 4. Discharge performance of AAFC

(A) U-I curves of the fuel cell in 2 M KOH electrolyte containing 0, 20, 60, and 100% ZnO.

(B) Discharge curves of fuel cell at current density of 20 mA/cm^2 in 2 M KOH electrolyte containing 0, and 100% ZnO.

(C) U-I curves of the fuel cell in 4 M KOH electrolyte containing 0, 20, 60, and 100% ZnO.

(D) Discharge curves of fuel cell at current density of 20 mA/cm^2 in 4 M KOH electrolyte containing 0, and 100% ZnO.

(E) U-I curves of the fuel cell in 6 M KOH electrolyte containing 0, 20, 60, and 100% ZnO.

(F) Discharge curves of fuel cell at current density of 20 mA/cm^2 in 6 M KOH electrolyte containing 0, and 100% ZnO.

During the discharge process, the Zn layer formed by the reaction between Al and $Zn(OH)_4^{2-}$ inhibits the Al self-corrosion, and also serves as the fuel for the later discharge of the fuel cell. In the perspective of energy, the Al-Zn energy transfer strategy, as a means of hydrogen suppression, temporarily stores part of the energy used by Al for hydrogen evolution in Zn, which reduces E_H and increases E_i. In short, the structure of mesh-encapsulated anode can strengthen the recycling of dead zinc, thereby improving the performance of the fuel cell. Besides, it can also ensure the stability of dead zinc participating in the reaction when the fuel cell is working under vibration and turbulence, which has a strong guiding significance for the application of AAFC in aviation, aerospace, navigation, and vehicle power.

Surface morphology characteristics of anode

Figures 5A–5C are the scanning electron microscope (SEM) images of Al alloy sheet immersed in 6 M KOH electrolytes containing ZnO with different PS for 1 h. Besides, the energy dispersive X-ray spectroscopy (EDS) results of the sampling points are shown in Table 3. When the PS of ZnO is 0%, the surface of the

Table 2. The discharge performance parameters of AAFC

Electrolyte (containing 100% ZnO)	Capacity Q (mAh/g)	Specific energy W (mWh/g)	Anode efficiency η_Q (%)	Fuel efficiency η_W (%)
2 M KOH (no mesh)	1296.576	1311.702	43.509	16.194
2 M KOH (with mesh)	1484.395	1498.822	49.812	18.504
4 M KOH (no mesh)	822.116	910.342	27.588	11.239
4 M KOH (with mesh)	1636.646	1815.378	54.921	22.412
6 M KOH (no mesh)	912.515	1037.857	30.621	12.813
6 M KOH (with mesh)	1839.842	2099.150	61.740	25.915

Al alloy sheet is eroded layer by layer and only scratches from mechanical polishing, so it is only shown in Figure S2. It can be seen from Figure 5A that when the PS of ZnO is 20%, the Zn film formed on the surface of the Al alloy sheet has many cracks and a large area of exposed Al. And the EDS results in Table 3 show that the proportion of Al element on the surface of the sampling point is about 29.73% at this time, whereas the Zn element is only 14.15%. They mean that the Zn film is relatively unstable and porous under this condition, and the exposed Al and crack areas will provide a greater possibility for the occurrence of Al self-corrosion. It can be seen from Figure 5B that when the PS of ZnO is 60%, the Zn film becomes thicker and denser, and has a tendency of depositing. The EDS results in Table 3 show that the proportion of Al element on the surface of the sampling point is gradually decreasing while the Zn element is increasing. They are also consistent with SEM description. It can be seen from Figure 5C that when the PS of ZnO is 100%, the Zn layer has been deposited, developed and accumulated continuously. At this time, the Al element on the surface of the sampling point only accounts for about 6.59%, while the Zn element reaches 54.26%. The possibility of Al self-corrosion is further reduced.

CONCLUSION

An aluminum-air fuel cell using a mesh-encapsulated anode was proposed in this work. The potassium hydroxide solution containing zinc oxide served as the electrolyte, which can realize energy redistribution. Besides, a structure of mesh-encapsulated anode was designed to utilize the energy of the dead zinc, which can highly improve performance of the fuel cell. The main conclusions are as follows:

(1) An aluminum-zinc energy transfer strategy was proposed to inhibit aluminum self-corrosion. When the concentration of potassium hydroxide in the electrolyte is 6 M and the percent saturation of zinc oxide is 100%, the hydrogen evolution of the aluminum is at the least. In this system, the hydrogen evolution rate is about 1.767×10^{-3} mg/cm^{2}s, and the inhibition efficiency is about 73.930%.

(2) A structure of mesh-encapsulated anode was designed to prevent the dead zinc from falling off, and improve energy utilization. When the fuel cell using mesh-encapsulated anode is discharged at 20 mA/cm^2 based on the energy redistribution strategy, the highest anode efficiency is up to 61.740%, and the fuel efficiency can reach 25.915%, which are respectively 2.016 and 2.022 times than those before optimization.

(3) A remarkable performance aluminum-air fuel cell can be obtained. When the fuel cell using mesh-encapsulated anode is discharged at 20 mA/cm^2 guided by energy redistribution strategy, the highest capacity is up to 1839.842 mAh/g, and the specific energy can reach 2099.150 mWh/g, which are respectively 101.623% and 102.258% higher than before optimization.

Limitations of the study

We have proposed an aluminum-air fuel cell using a mesh-encapsulated anode based on the energy redistribution strategy to improve the discharge performance of the fuel cell. However, only zinc oxide is used as the medium of aluminum-zinc energy transfer and is added to the alkaline electrolyte in this study. It lacks a further discussion on the universality of the energy redistribution strategy, and it needs further analysis in the future.

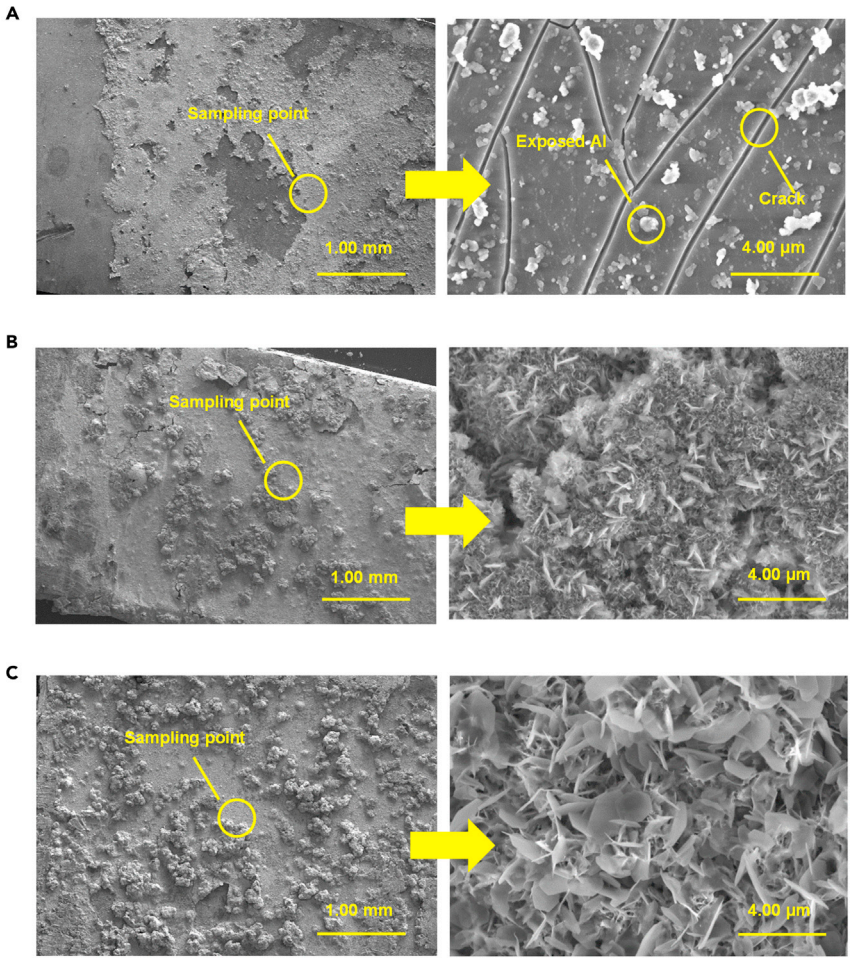

Figure 5. The SEM of Al alloy sheet immersed in 6 M KOH electrolyte containing ZnO with different PS for 1 h

(A) SEM image of Al alloy sheet immersed in 6 M KOH electrolyte containing 20% ZnO.

(B) SEM image of Al alloy sheet immersed in 6 M KOH electrolyte containing 60% ZnO.

(C) SEM image of Al alloy sheet immersed in 6 M KOH electrolyte containing 100% ZnO.

STAR★METHODS

Detailed methods are provided in the online version of this paper and include the following:

- KEY RESOURCES TABLE
- RESOURCE AVAILABILITY
  - Lead contact
  - Materials availability
  - Data and code availability
- METHOD DETAILS
  - Preparation of electrodes and electrolyte

Table 3. The EDS of Al alloy sheet immersed in 6 M KOH electrolyte containing ZnO with different PS for 1 h

Composition (%)	20% ZnO	60% ZnO	100% ZnO
O	56.12	44.12	39.15
Al	29.73	11.25	6.59
Zn	14.15	44.63	54.26

- Hydrogen evolution test
- Electrochemical measurement
- Performance measurement
- Surface micro-morphology test

SUPPLEMENTAL INFORMATION

Supplemental information can be found online at https://doi.org/10.1016/j.isci.2021.103259.

ACKNOWLEDGMENTS

This work is supported by the National Natural Science Foundation of China (No.21706013), the State Key Laboratory of Automotive Safety and Energy Project (No. KF2024), the Beijing Student's Innovation and Entrepreneurship Training Program Project (No. S202110007088), and the Beijing Institute of Technology Student's Innovation and Entrepreneurship Training Program Project (No. BIT262201109). The team wishes to Analysis & Testing Center, Beijing Institute of Technology providing material characterizations.

AUTHOR CONTRIBUTIONS

M. W. proposed the idea, and completed the writing and revision of the paper. K. W., and P. P. guided the research direction and reviewed the paper. M. W., Y. Z., P. Z., and Y. L. conducted experiments of TPC, EIS, SEM, and EDS. M. W., and J. L. designed and laid out the style and color of the figures in the paper, and completed the hydrogen evolution test and OCP experiment. S. Z., and J. C. corrected the language of the paper.

DECLARATION OF INTERESTS

The authors declare no competing interests.

Received: July 28, 2021
Revised: September 27, 2021
Accepted: October 8, 2021
Published: November 19, 2021

REFERENCES

Chen, D., Rui, X., Zhang, Q., Geng, H., Gan, L., Zhang, W., Li, C., Huang, S., and Yu, Y. (2019). Persistent zinc-ion storage in mass-produced V_2O_5 architectures. Nano Energy *60*, 171–178. https://doi.org/10.1016/j.nanoen.2019.03.034.

Eaves-Rathert, J., Moyer, K., Zohair, M., and Pint, C.L. (2020). Kinetic- versus diffusion-driven three-dimensional growth in magnesium metal battery anodes. Joule *4*, 1324–1336. https://doi.org/10.1016/j.joule.2020.05.007.

Fan, L., Lu, H., and Leng, J. (2015). Performance of fine structured aluminum anodes in neutral and alkaline electrolytes for Al-air batteries. Electrochim. Acta *165*, 22–28. https://doi.org/10.1016/j.electacta.2015.03.002.

Feng, S., Yang, G., Zheng, D., Wang, L., Wang, W., Wu, Z., and Liu, F. (2020). A dual-electrolyte aluminum/air microfluidic cell with enhanced voltage, power density and electrolyte utilization via a novel composite membrane. J. Power Sources *478*, 228960. https://doi.org/10.1016/j.jpowsour.2020.228960.

Gao, Y., Du, X., Hou, Z., Shen, X., Mai, Y.-W., Tarascon, J.-M., and Zhang, B. (2021). Unraveling the mechanical origin of stable solid electrolyte interphase. Joule. https://doi.org/10.1016/j.joule.2021.05.015.

Gelman, D., Lasman, I., Elfimchev, S., Starosvetsky, D., and Ein-Eli, Y. (2015). Aluminum corrosion mitigation in alkaline electrolytes containing hybrid inorganic/organic inhibitor system for power sources applications. J. Power Sources *285*, 100–108. https://doi.org/10.1016/j.jpowsour.2015.03.048.

Goel, P., Dobhal, D., and Sharma, R.C. (2020). Aluminum–air batteries: a viability review. J. Energy Storage *28*, 101287. https://doi.org/10.1016/j.est.2020.101287.

Hannula, I., and Reiner, D.M. (2019). Near-term potential of biofuels, electrofuels, and battery electric vehicles in decarbonizing road transport. Joule *3*, 2390–2402. https://doi.org/10.1016/j.joule.2019.08.013.

Jiang, H., Yu, S., Li, W., Yang, Y., Yang, L., and Zhang, Z. (2020). Inhibition effect and mechanism of inorganic–organic hybrid additives on three-dimension porous aluminum foam in alkaline Al–air battery. J. Power Sources *448*, 227460. https://doi.org/10.1016/j.jpowsour.2019.227460.

Jin, Y., Liu, K., Lang, J., Jiang, X., Zheng, Z., Su, Q., Huang, Z., Long, Y., Wang, C.-a., Wu, H., and Cui, Y. (2020). High-energy-density solid-electrolyte-based liquid Li-S and Li-Se batteries. Joule *4*, 262–274. https://doi.org/10.1016/j.joule.2019.09.003.

Lee, W.-H., Choi, S.-R., and Kim, J.-G. (2020). Effect of agar as electrolyte additive on the aluminum–air batteries. J. Electrochem. Soc. *167*, 110503. https://doi.org/10.1149/1945-7111/ab9cc7.

Lin, M.C., Gong, M., Lu, B., Wu, Y., Wang, D.Y., Guan, M., Angell, M., Chen, C., Yang, J., Hwang, B.J., and Dai, H. (2015). An ultrafast rechargeable aluminium-ion battery. Nature *520*, 325–328. https://doi.org/10.1038/nature14340.

Mokhtar, M., Majlan, E.H., Ahmad, A., Tasirin, S.M., and Daud, W.R.W. (2018). Effect of ZnO filler on PVA-alkaline solid polymer electrolyte for aluminum–air battery applications. J. Electrochem. Soc. *165*, A2483–A2492. https://doi.org/10.1149/2.0381811jes.

Nie, Y., Gao, J., Wang, E., Jiang, L., An, L., and Wang, X. (2017). An effective hybrid organic/inorganic inhibitor for alkaline aluminum–air fuel cells. Electrochim. Acta *248*, 478–485. https://doi.org/10.1016/j.electacta.2017.07.108.

Pan, L., Chen, D., Pei, P., Huang, S., Ren, P., and Song, X. (2021). A novel structural design of air cathodes expanding three-phase reaction interfaces for zinc-air batteries. Appl. Energy *290*, 116777. https://doi.org/10.1016/j.apenergy.2021.116777.

Qiao, Y., Wang, Q., Mu, X., Deng, H., He, P., Yu, J., and Zhou, H. (2019). Advanced hybrid electrolyte Li-O_2 battery realized by dual superlyophobic membrane. Joule *3*, 2986–3001. https://doi.org/10.1016/j.joule.2019.09.002.

Sun, P., Chen, J., Huang, Y., Tian, J.-H., Li, S., Wang, G., Zhang, Q., Tian, Z., and Zhang, L. (2021). High-Strength agarose gel electrolyte enables long-endurance wearable Al–air batteries with greatly suppressed self-corrosion. Energy Storage Mater. *34*, 427–435. https://doi.org/10.1016/j.ensm.2020.10.009.

Tan, P., Jiang, H.R., Zhu, X.B., An, L., Jung, C.Y., Wu, M.C., Shi, L., Shyy, W., and Zhao, T.S. (2017). Advances and challenges in lithium–air batteries. Appl. Energ. *204*, 780–806. https://doi.org/10.1016/j.apenergy.2017.07.054.

Tan, P., Shyy, W., Zhao, T.S., Zhang, R.H., and Zhu, X.B. (2016). Effects of moist air on the cycling performance of non-aqueous lithium–air batteries. Appl. Energ. *182*, 569–575. https://doi.org/10.1016/j.apenergy.2016.08.113.

Tian, Y., Sun, Y., Hannah, D.C., Xiao, Y., Liu, H., Chapman, K.W., Bo, S.-H., and Ceder, G. (2019). Reactivity-guided Interface design in Na metal solid-state batteries. Joule *3*, 1037–1050. https://doi.org/10.1016/j.joule.2018.12.019.

Wang, F., Borodin, O., Ding, M.S., Gobet, M., Vatamanu, J., Fan, X., Gao, T., Eidson, N., Liang, Y., Sun, W., et al. (2018a). Hybrid aqueous/non-aqueous electrolyte for safe and high-energy Li-ion batteries. Joule *2*, 927–937. https://doi.org/10.1016/j.joule.2018.02.011.

Wang, K., Pei, P., Wang, Y., Liao, C., Wang, W., and Huang, S. (2018b). Advanced rechargeable zinc-air battery with parameter optimization. Appl. Energ. *225*, 848–856. https://doi.org/10.1016/j.apenergy.2018.05.071.

Wang, K., Xiao, Y., Liu, X., Zhang, Z., Chen, J., Zuo, Y., and Zhao, S. (2020a). Performance improvement of underwater Mg–Oxygen battery with parameter optimization. J. Electrochem. Soc. *167*. https://doi.org/10.1149/1945-7111/abc90b.

Wang, K., Zuo, Y., Pei, P., Liu, X., Wei, M., Xiao, Y., Xiong, J., and Zhang, P. (2021). Zn–Ni reaction in the alkaline zinc-air battery using a nickel-supported air electrode. Mater. Today Energy *21*, 100823. https://doi.org/10.1016/j.mtener.2021.100823.

Wang, L., Cheng, R., Liu, C., Ma, M.C., Wang, W., Yang, G., Leung, M.K.H., Liu, F., and Feng, S.P. (2020b). Trielectrolyte aluminum–air cell with high stability and voltage beyond 2.2 V. Mater. Today Phys. *14*, 100242. https://doi.org/10.1016/j.mtphys.2020.100242.

Wang, Q., Miao, H., Xue, Y., Sun, S., Li, S., and Liu, Z. (2017). Performances of an Al–0.15 Bi–0.15 Pb–0.035 Ga alloy as an anode for Al–air batteries in neutral and alkaline electrolytes. RSC Adv. *7*, 25838–25847. https://doi.org/10.1039/c7ra02918g.

Wang, Y., Kwok, H.Y.H., Pan, W., Zhang, H., Lu, X., and Leung, D.Y.C. (2019a). Parametric study and optimization of a low-cost paper-based Al–air battery with corrosion inhibition ability. Appl. Energy *251*, 113342. https://doi.org/10.1016/j.apenergy.2019.113342.

Wang, Y., Kwok, H.Y.H., Pan, W., Zhang, Y., Zhang, H., Lu, X., and Leung, D.Y.C. (2020c). Printing Al–air batteries on paper for powering disposable printed electronics. J. Power Sources *450*, 227685. https://doi.org/10.1016/j.jpowsour.2019.227685.

Wang, Y., Pan, W., Kwok, H.Y.H., Zhang, H., Lu, X., and Leung, D.Y.C. (2019b). Liquid-free Al–air batteries with paper-based gel electrolyte: a green energy technology for portable electronics. J. Power Sources *437*, 226896. https://doi.org/10.1016/j.jpowsour.2019.226896.

Wu, F., and Yu, Y. (2018). Toward true lithium–air batteries. Joule *2*, 815–817. https://doi.org/10.1016/j.joule.2018.04.019.

Wu, P., Wu, S., Sun, D., Tang, Y., and Wang, H. (2020a). A review of Al alloy anodes for Al–air batteries in neutral and alkaline aqueous electrolytes. Acta Metall. Sin. *34*, 309–320. https://doi.org/10.1007/s40195-020-01140-x.

Wu, S., Hu, S., Zhang, Q., Sun, D., Wu, P., Tang, Y., and Wang, H. (2020b). Hybrid high-concentration electrolyte significantly strengthens the practicability of alkaline aluminum-air battery. Energy Storage Mater. *31*, 310–317. https://doi.org/10.1016/j.ensm.2020.06.024.

Wu, Z., Zhang, H., Yang, D., Zou, J., Qin, K., Ban, C., Cui, J., and Nagaumi, H. (2020c). Electrochemical behaviour and discharge characteristics of an Al–Zn–In–Sn anode for Al–air batteries in an alkaline electrolyte. J. Alloys Compd. *837*. https://doi.org/10.1016/j.jallcom.2020.155599.

Yang, L., Wu, Y., Chen, S., Xiao, Y., Chen, S., Zheng, P., Wang, J., and Qu, J.-E. (2021). A promising hybrid additive for enhancing the performance of alkaline aluminum–air batteries. Mater. Chem. Phys. *257*, 123787. https://doi.org/10.1016/j.matchemphys.2020.123787.

Yu, J., Hu, Z., and Du, Z. (2020a). Electrochemical performance and interface analysis of Al–MgO composite anodes for Al–air batteries. J. Electrochem. Soc. *167*, 140514. https://doi.org/10.1149/1945-7111/abc10b.

Yu, S., Yang, X., Liu, Y., Zhan, F., Wen, Q., Li, J., and Li, W. (2020b). High power density Al-air batteries with commercial three-dimensional aluminum foam anode. Ionics *26*, 5045–5054. https://doi.org/10.1007/s11581-020-03618-1.

Zhang, P., Wang, K., Pei, P., Zuo, Y., Wei, M., Liu, X., Xiao, Y., and Xiong, J. (2021). Selection of hydrogel electrolytes for flexible zinc–air batteries. Mater. Today Chem. *21*, 100538. https://doi.org/10.1016/j.mtchem.2021.100538.

Zhang, Z., Zuo, C., Liu, Z., Yu, Y., Zuo, Y., and Song, Y. (2014). All-solid-state Al–air batteries with polymer alkaline gel electrolyte. J. Power Sources *251*, 470–475. https://doi.org/10.1016/j.jpowsour.2013.11.020.

Zhao, R., Xie, J., Wen, H., Wang, F., Yang, J., and Zhang, D. (2020). Performance modeling and parameter sensitivity analyses of an aluminum–air battery with dual electrolyte structure. J. Energy Storage *32*, 101696. https://doi.org/10.1016/j.est.2020.101696.

Zhu, C., Yang, H., Wu, A., Zhang, D., Gao, L., and Lin, T. (2019). Modified alkaline electrolyte with 8-hydroxyquinoline and ZnO complex additives to improve Al–air battery. J. Power Sources *432*, 55–64. https://doi.org/10.1016/j.jpowsour.2019.05.077.

Zuo, Y., Wang, K., Pei, P., Wei, M., Liu, X., Xiao, Y., and Zhang, P. (2021). Zinc dendrite growth and inhibition strategies. Mater. Today Energy *20*, 100692. https://doi.org/10.1016/j.mtener.2021.100692.

STAR★METHODS

KEY RESOURCES TABLE

REAGENT or RESOURCE	SOURCE	IDENTIFIER
Chemicals, peptides, and recombinant proteins		
1060 Al alloy plate (≥99.6%)	Shenzhen Shengjili Co., Ltd	N/A
KOH (≥85.0%)	Tianjin Damao Chemical Reagent Co., Ltd	CAS-1310-58-3
ZnO (≥99.0%)	Tianjin Zhiyuan Chemical Reagent Co., Ltd	LOT-2018091062
Deionized water	Shanghai Tian Scientific Co., Ltd	CAS-7732-18-5
Mesh, 1.5 ×1.5 mm, 06Cr19Ni10	ZENG NIU	ZN-8002
Carbon nanotubes	Hengqiu Tech. Inc.	CNTS-010-0
Graphene	TIME SNANO	MFG-TNNFA5
Waterproof layer	QUANTUM SPHERE	LOT-080220-13-01

RESOURCE AVAILABILITY

Lead contact

Further information and requests for resources should be directed to and will be fulfilled by the lead contact, Keliang Wang (wangkl@bit.edu.cn).

Materials availability

This study did not generate new unique reagents.

Data and code availability

- All data reported in this paper will be shared by the lead contact upon request.
- This paper does not report original code.
- Any additional information required to reanalyze the data reported in this paper is available from the lead contact upon request.

METHOD DETAILS

Preparation of electrodes and electrolyte

The thickness of the Al alloy plate was 0.6 mm, and the composition was shown in Table S1. Before the experiment, the Al alloy plate of specific size was polished with 320# sandpaper, and then washed with deionized water (Nie et al., 2017). KOH and ZnO were weighed and dissolved in deionized water to form 12 mixed solutions, which the concentration of OH^- was 2, 4, and 6 M and the PS of Zn^{2+} was 0, 20, 60, and 100%. The catalyst was prepared by hydrothermal reaction of carbon-containing substances such as carbon nanotubes and graphene (Wang et al., 2021). The air electrode composed of catalyst, waterproof layer and foamed nickel was pressed by a roller press (Pan et al., 2021).

Hydrogen evolution test

At 20°C, the hydrogen evolution test of Al was carried out using instruments such as beaker, glass slide, water tank and scale (the graduation value was 10^{-4} g). Firstly, Al alloy sheets (5.0 cm × 2.0 cm × 0.06 cm) were immersed in the beakers containing the above 12 groups of solutions. Then, glass slides were placed on each beaker to reduce the loss of vapor. Finally, the beakers were placed in a water tank at 20°C, and the total mass of the systems was measured every 5 minutes for a total of 60 minutes. According to the above test, the mass of hydrogen evolution for the Al alloy sheet per unit time could be obtained through Equation 5, and then the hydrogen evolution rate and inhibition efficiency could be calculated as Equations 6 and 7 (Lee et al., 2020):

$$\Delta m_H = m_a^{n+1} - m_a^n (n = 0, 1, \cdots, 11) \quad \text{(Equation 5)}$$

$$v = \frac{\Delta m_H}{S \cdot \Delta t_H} \quad \text{(Equation 6)}$$

$$\eta_H = \frac{\Delta v}{v_0} \times 100\% \quad \text{(Equation 7)}$$

Where Δm_H is the mass of hydrogen evolution per unit time (mg); m_a is the total mass of the system (mg); v is the hydrogen evolution rate (mg/cm^{2}s); S is the surface area of the Al alloy plate immersed in the electrolyte (cm^2); Δt_H is the measurement time interval (5 min); η_H is the inhibition efficiency per unit time (%); and v_0 is the hydrogen evolution rate in KOH solution containing 0% ZnO.

Electrochemical measurement

The electrochemical measurement was executed in a three-electrode system using CHI660E electrochemical workstation (Shanghai Chenhua Instrument Co., Ltd.) at 20°C. The Al alloy sheet (1.0 cm × 1.0 cm × 0.06 cm) was used as the working electrode, the platinum sheet (1.5 cm × 1.5 cm × 0.05 cm) was the auxiliary electrode, and the Hg/HgO (1 M KOH) was the reference electrode (Zhu et al., 2019). Before the test, the Al alloy sheet was immersed in the solution for 500 s to obtain a stable reaction state, and the change of OCP during this period of time was measured. And then, the TPC in the range of −1.75 V to −1.25 V at a scanning frequency of 5 mV/s was measured to obtain the equilibrium potential and corrosion current of Al in different electrolytes. Finally, EIS in the frequency range of 0.1–100 kHz at an AC amplitude of 5 mV/was recorded based on the steady-state OCP (Wang et al., 2019a).

Performance measurement

The discharge performance of AAFC was tested using the NEWARE BTS 7.5X. Firstly, the U-I curves from 0 to 60 mA/cm^2 based on the above 12 groups of electrolytes were analyzed. The test step was 10 mA/cm^2 and the time interval was 300 s. Then, the discharge experiment of AAFC with and without a mesh at a current density of 20 mA/cm^2 was conducted until the voltage was close to 0. The Al alloy sheet (1.0 cm × 0.8 × cm × 0.06 cm) was used as anode and 2, 4, and 6 M KOH solutions containing 0 and 100% ZnO were used as the electrolytes. Anode efficiency and fuel efficiency of the fuel cell after each experiment were calculated as Equations 8 and 9 (Wang et al., 2017):

$$\eta_Q = \frac{Q}{Q_{Al}} \times 100\% \quad \text{(Equation 8)}$$

$$\eta_W = \frac{W}{W_{Al}} \times 100\% \quad \text{(Equation 9)}$$

Of these:

$$Q = \frac{I\Delta t_d}{\Delta m_{Al}} \quad \text{(Equation 10)}$$

$$W = \frac{UI\Delta t_d}{\Delta m_{Al}} \quad \text{(Equation 11)}$$

Where Q and W are the actual capacity (mAh/g) and specific energy (mWh/g) of the fuel cell respectively; Q_{Al} and W_{Al} are the theoretical capacity and specific energy of the fuel cell, which are about 2980 mAh/g and 8100 mWh/g respectively; I is the discharge current (mA); Δt_d is the discharge time (h); Δm_{Al} is the mass of the anode consumed (g); and U is the discharge voltage (V).

Surface micro-morphology test

The pre-treated Al alloy sheet (0.5 cm × 0.5 cm × 0.06 cm) was immersed in the electrolytes for 1 h. After it was taken out, washed with deionized water and dried in high temperature box (Wang et al., 2020c). The surface microstructure was inspected by Regulus 8230 SEM, and then the surface element was quantitatively analyzed through EDS.